

Geophysical Research Letters[®]



RESEARCH LETTER

10.1029/2023GL107324

Strain Partitioning and Fault Kinematics in the Northern Qilian Shan (NE Tibet) Determined From Bayesian Inference of Geodetic Data

Yingfeng Zhang¹ , Sam Wimpenny² , Luca Dal Zilio^{3,4} , and Xinjan Shan¹ 

¹State Key Laboratory of Earthquake Dynamics, Institute of Geology, China Earthquake Administration, Beijing, China, ²COMET, School of Earth Sciences, University of Bristol, Bristol, UK, ³Earth Observatory of Singapore, Nanyang Technological University, Singapore, Singapore, ⁴Asian School of the Environment, Nanyang Technological University, Singapore, Singapore

Key Points:

- Oblique convergence in the northern Qilian Shan is accommodated by sub-parallel thrust and strike-slip faulting
- The short-term geodetic measurements do not constrain the thrust fault kinematics in the northern Qilian Shan over geological timescales
- Multi-fault earthquakes may be common in the region as all of the shallow thrust faults are linked together by locked fault segments

Supporting Information:

Supporting Information may be found in the online version of this article.

Correspondence to:

Y. Zhang,
jingqing129@gmail.com

Citation:

Zhang, Y., Wimpenny, S., Dal Zilio, L., & Shan, X. (2024). Strain partitioning and fault kinematics in the northern Qilian Shan (NE Tibet) determined from Bayesian inference of geodetic data. *Geophysical Research Letters*, 51, e2023GL107324. <https://doi.org/10.1029/2023GL107324>

Received 14 NOV 2023

Accepted 8 APR 2024

Author Contributions:

Conceptualization: Yingfeng Zhang, Sam Wimpenny

Formal analysis: Sam Wimpenny, Luca Dal Zilio

Funding acquisition: Xinjan Shan

Methodology: Yingfeng Zhang, Sam Wimpenny

Project administration: Xinjan Shan

Writing – original draft: Yingfeng Zhang

Writing – review & editing:

Yingfeng Zhang, Sam Wimpenny, Luca Dal Zilio, Xinjan Shan

Abstract Oblique convergence across the northern Qilian Shan is accommodated by sub-parallel strike-slip and thrust faults that ruptured simultaneously in the Mw 8 Gulang earthquake in 1927. We investigate the kinematics of fault loading in the northern Qilian Shan and provide insights into the conditions necessary for generating multi-fault earthquakes. We perform Bayesian inversions for the geometry and creep rate on the fault network. We infer that all of the thrust faults are locked north of the Qilian-Haiyuan strike-slip fault and are accumulating elastic strain. Multi-fault earthquakes may occur in this fault system because the faults are simultaneously loaded by the same source of deformation and are linked together by locked fault segments. The interseismic velocity field alone can not contain the location or activity of individual faults visible in the geomorphology, therefore the short-term geodetic measurements may not reliably indicate the long-term behavior of the fault system.

Plain Language Summary This study aims to understand the earthquake hazard in the northern Qilian region of China. We use measurements of ground deformation between earthquakes to infer how the faults are being loaded in the region. We find that the ground deformation can be explained by a simple model with a single, slowly creeping fault at depth that loads all of the overlying faults. Large earthquakes that were caused by slip on many different faults at the same time have occurred in this region before. We suggest these so-called “multi-fault” earthquakes may occur because all of the faults are being simultaneously loaded by the same source of stress.

1. Introduction

Where convergence between a mountain range and its foreland is oblique the long-term deformation is often accommodated by a combination of thrust faulting along the range margins and strike-slip faulting within its interior—a kinematic configuration known as strain partitioning (Daout et al., 2016; McCaffrey, 1988; Murphy et al., 2014; Sanderson & Marchini, 1984; Schütt & Whipp, 2020). Faults accommodating strain partitioning can slip in individual earthquakes releasing strain piecemeal, or in multi-fault earthquakes that rupture thrust and strike-slip faults simultaneously releasing the strain in one large event (e.g., 2016 Mw 7.8 Kaikoura earthquake; Herman et al., 2023; Shi et al., 2017).

An important question in forecasting seismic hazard in zones of strain partitioning is whether we can determine the conditions necessary for generating multi-fault earthquakes from surface observations. One approach to this problem has been to study how elastic strain is accumulating in regions where multi-fault earthquakes have occurred in the past (Avouac, 2015; Dal Zilio et al., 2020, 2021). Such studies tentatively indicate that multi-fault earthquakes have ruptured fault systems that were entirely locked above a certain depth and were being loaded by a single creeping décollement at depth (Lamb, 2021; Lamb et al., 2018).

In this study, we consider the northern Qilian Shan strain-partitioned fault system, which consists of north-vergent thrusts and ~E-W trending strike-slip faults that accommodate the oblique convergence between the Gobi Alashan and the Qilian Shan (Figure 1; Allen et al., 2017; Daout et al., 2017; Luo & Wang, 2022). These faults have ruptured in recent destructive earthquakes (Guo et al., 2020; Y. Zhang et al., 2020; Y. Zhang, Chen et al., 2023; Y. Zhang, Wimpenny et al., 2023). Paleo-earthquake research indicates that multi-fault ruptures that

© 2024. The Authors.

This is an open access article under the terms of the [Creative Commons](https://creativecommons.org/licenses/by/4.0/)

[Attribution-NonCommercial-NoDerivs](https://creativecommons.org/licenses/by/4.0/)

License, which permits use and

distribution in any medium, provided the

original work is properly cited, the use is

non-commercial and no modifications or

adaptations are made.

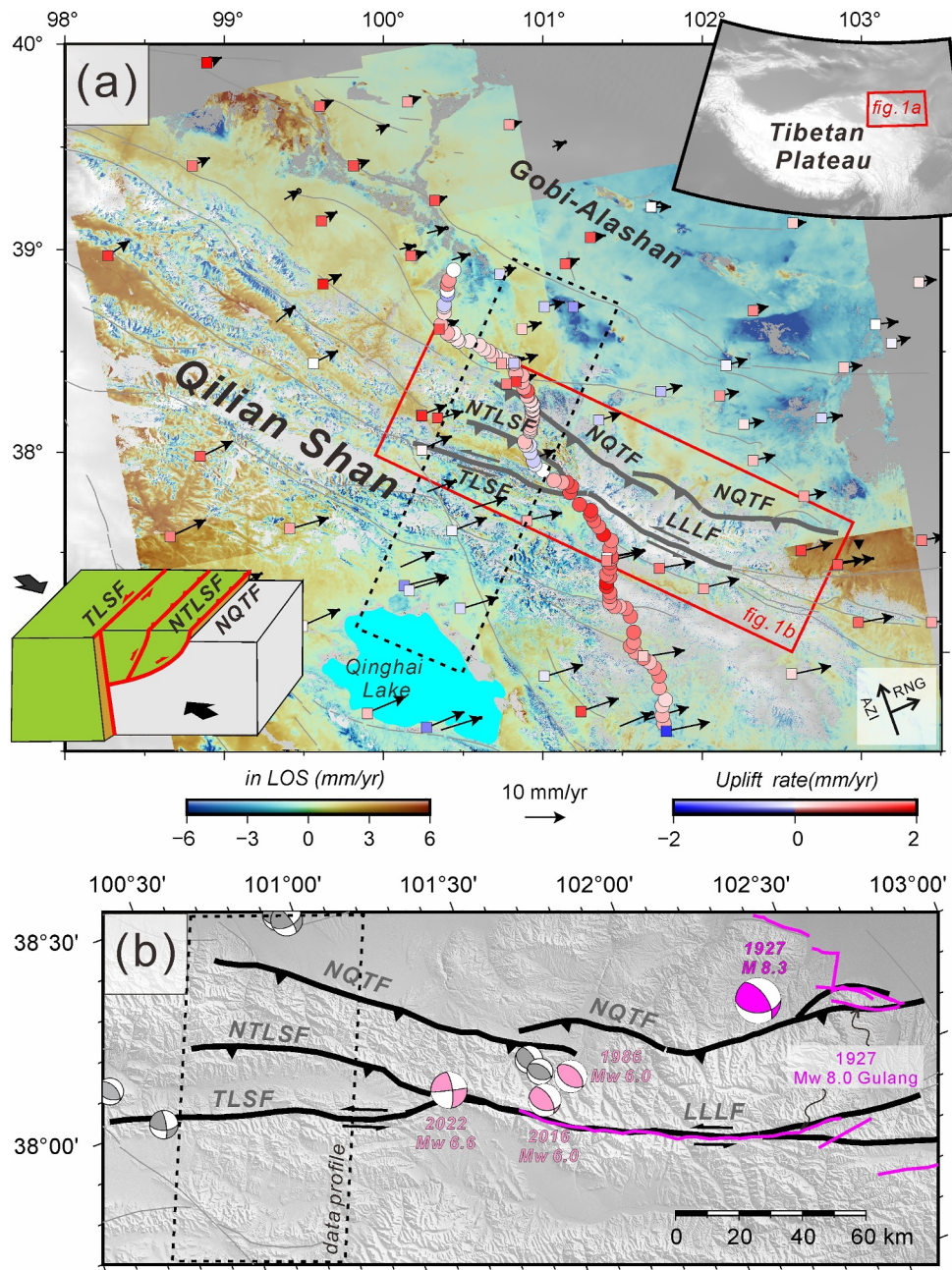


Figure 1. Geodetic measurements and seismotectonic setting. (a) Geodetic data including InSAR (Ou et al., 2022), GNSS horizontal and vertical components (black arrows and colored squares; Wang & Shen, 2020; Zhao et al., 2023), and leveling data (colored circles; Y. Wu et al., 2022). Dashed black box indicates data cross-section for 2-D fault model. Bold gray lines show the northern Qilian strain-partitioned fault system. The insert cartoon illustrates kinematics of this system. (b) Active faults and historical earthquakes in the area. Black lines denote faults; pink lines show 1927 Mw 8.0 Gulang earthquake ruptures (Allen et al., 2017; Guo et al., 2020). Focal mechanisms from Gaudemer et al. (1995) and USGS.

span the strike-slip and thrust faults have also occurred on this fault system in the past and may even repeat every ~4,000 years (Gao et al., 2022; Z. Li et al., 2022).

We compile geodetic measurements of interseismic ground deformation from InSAR, GNSS and leveling and assess whether they can constrain the distribution of creeping and locked fault segments within the northern Qilian Shan. We take a Bayesian approach to the problem, as this provides posterior probability distributions for the free parameters that define the kinematic models and allows us to quantitatively assess their uncertainties

given the data and prior information available. Finally, we consider the implications of our models for fault loading in the Qilian Shan.

2. Tectonic Setting and Interseismic Deformation in the Northern Qilian Shan

2.1. Tectonic Setting

The Qilian Shan is a WNW-ESE trending mountain range that lies north of the Tibetan Plateau, between the Qaidam Basin to the south and the Gobi Alashan to the north (Figure 1). A mixture of strike-slip and thrust-faulting earthquake focal mechanisms indicate that the northern margin of the Qilian Shan is accommodating oblique shortening (Figure 1). North-vergent thrusts known as the North Qilian thrust fault (NQTF) and North Tuolaishan thrust fault (NTLSF) lie along the northern margin of the range and accommodate range-perpendicular shortening (Luo & Wang, 2022). WNW-ESE trending strike-slip faults, including the Lenglongling fault (LLLF) and Tuolaishan fault (TLSF), cut across the interior of the range and accommodate range-parallel shear (Gaudemer et al., 1995; Lasserre et al., 2002).

Geological reconstructions, modeling of GNSS velocities, and seismic tomographic imaging have led to the interpretation that the thrust faults root into a south-dipping décollement at ~15–25 km depth with a dip angle of 10–20° (Allen et al., 2017; Daout et al., 2017; Gaudemer et al., 1995; Meyer et al., 1998; Shen et al., 2017; Ye et al., 2015). Paleo-earthquakes are inferred to have sometimes independently, and sometimes simultaneously, ruptured the strike-slip and thrust faults (see Figure 1b; Z. Li et al., 2022; Gao et al., 2022; Guo et al., 2020).

Estimates of the Late Quaternary cumulative shortening rate across all of the range-front thrust faults are 3–4 mm/yr (Xiong et al., 2017; Zhong et al., 2020). Estimates of the rate of strike-slip motion on the Qilian-Haiyuan fault averaged over the Late Quaternary are 3.3–7.1 mm/yr on the TLSF and LLLF segment (W. G. He et al., 2010; Jiang et al., 2017; Yuan et al., 2013; P. Zhang et al., 2004; Zheng et al., 2013).

2.2. Geodetic Measurements of Interseismic Deformation

To constrain the 3-dimensional interseismic velocity field in the northern Qilian Shan, we combine GNSS, InSAR and leveling measurements collected over the past 20 years (Figure 1 and Figure S1 and Table S1 in Supporting Information S1).

The horizontal velocities are the GNSS solutions formulated by Wang and Shen (2020). The measurements derive from both campaign-style and continuous GNSS networks occupied over the period 1999–2016. Non-tectonic signals and earthquake-related deformation have been removed from the time-series (Wang & Shen, 2020). The typical uncertainties in the horizontal velocities are 0.5 mm/yr.

We complement the GNSS data with the dense (500 m pixel size) InSAR line-of-sight velocity field of Ou et al. (2022) derived from ascending- and descending-track Sentinel-1 data covering the time period 2014–2019. The InSAR velocity field has been tied to the GNSS reference frame of Wang and Shen (2020). Short-wavelength line-of-sight displacement signals related to mining, hydrological loading and permafrost freeze-thaw are contained within the dataset, along with longer-wavelength deformation associated with tectonic loading.

Finally, we used measurements of vertical velocities from both GNSS and leveling. The GNSS vertical velocities consist of 113 continuous and 969 campaign observations spanning 2008–2019 (Zhao et al., 2023). Postseismic effects were mitigated by discarding stations that contain offsets and transients around the timing of large earthquakes. We also included the vertical velocities derived from repeat occupation of leveling lines from Y. Wu et al. (2022). The leveling lines were occupied first in 2012 and then again in 2015.

The GNSS velocity field is dominated by a broad decrease in the north-eastward directed velocities from the interior of the Qilian Shan near Qinghai Lake toward the Gobi Alashan, with the largest velocity gradients across the northern margin of the Qilian Shan (Figure 1). The InSAR LOS velocity field contains significant scatter, but in the long-wavelength component there is a 3–5 mm/yr increase in the ascending-track LOS velocity, and decrease in the descending-track LOS velocity, from SW to NE across the northern margin of the Qilian Shan. The leveling data contain large uncertainties but indicate a small change in the rate of uplift across the northern margin of the Qilian Shan of around 2 ± 1.3 mm/yr. Overall, the geodetic observations indicate that the highest gradients in velocity, and therefore highest strain rates, occur across the northern margin of the Qilian Shan across the strain-partitioned fault system.

3. Modeling the Interseismic Deformation

3.1. Model Setup

We interpret the spatial correlation between the broad velocity gradients in the geodetic data and the major active faults along the northern Qilian Shan to reflect elastic strain accumulation around the mapped faults driven by creep on their underlying shear zones. In this section, we follow an approach similar to Daout et al. (2016) and attempt to recover information about the locations of the creeping shear zone that load the shallower locked fault using measurements of the interseismic velocity field.

Given the along-strike simplicity of the fault system and the velocity field, we consider only a two-dimensional model. For each creeping fault included in the model, we assume it is planar and that it has a single creeping-to-locked transition at its up-dip end. We model the surface velocity field caused by creeping fault segments using linear combinations of the analytical solutions for the deformation around edge dislocations in a 2-dimensional, linearly elastic half-space (Segall, 2010). Where a single fault bifurcates into two faults, we follow Daout et al. (2016) and assume that there must be kinematic compatibility across the fault triple junction such that the horizontal and vertical components of the velocity field are conserved.

The free parameters in this problem are the geometries of the faults in the subsurface, their creep rates, and the position of the locked-to-creeping transition on each fault. We also include a constant offset applied to each dataset (GNSS, InSAR, leveling) to account for reference frame differences. In order to solve for these free parameters we employ a Bayesian inversion implemented in the software package Flower2D (Daout et al., 2016, 2017). Flower2D randomly samples the prior distributions and uses the Metropolis algorithm to evaluate the posterior probability density functions (PDFs), guided by the geodetic data and uncertainties.

The uncertainties in the InSAR and GNSS datasets are comparable (Figure S5 in Supporting Information S1); Therefore, we used the square root of the relative number of data points as a weighting factor in our inversions (Ou et al., 2022), which is equivalent to a weight of 20 to the GNSS and leveling data and a weight of 1 to the InSAR data. The leveling data have much larger uncertainties than the InSAR and GNSS velocities (Figure S5 in Supporting Information S1), though we found that removing the leveling data from the inversions had little effect on the results (Figures S7 and S8 in Supporting Information S1).

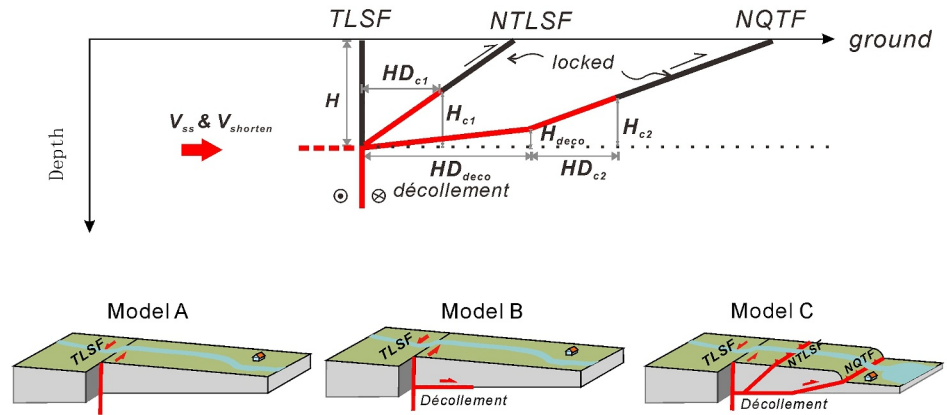
We first attempt to model the velocity field assuming that the surface deformation is a result of creep on a fault that has its up-dip edge beneath the TLSF (Model A; Figure 2a). The range-parallel component of motion is accommodated by a vertical strike-slip fault that is locked from the surface down to a depth H , below which is a semi-infinite dislocation creeping at a velocity V_{ss} . Crustal shortening rate is accommodated by a horizontal semi-infinite dislocation at depth H creeping at a rate $V_{shorten}$ that terminates against the TLSF. Changes in the dip of the creeping strike-slip fault have no effect on the range-perpendicular velocities, and therefore our two-fault configuration also simulates oblique slip on a décollement south of the TLSF.

We then consider models with increasing numbers of creeping faults to examine the sensitivity of the velocity field measurements to the complexity of the fault system at depth. The additional complexity we consider in Model B is that we added a creeping décollement to the north of the TLSF (Model B; Figure 2). In Model B, both the down-dip extension of the TLSF, and some portion of the décollement north of the TLSF, can creep. The additional parameters in Model B are the width of the décollement HD_{deco} and its height H_{deco} . In Model C we introduce further complexity by including two ramp faults that extend from the décollement to the surface where the NQTF and NTLFS outcrop (Model C; Figure 2). Model C therefore has four additional free parameters: the widths $HD_{c1,2}$ and heights $H_{c1,2}$ of the two ramp thrusts.

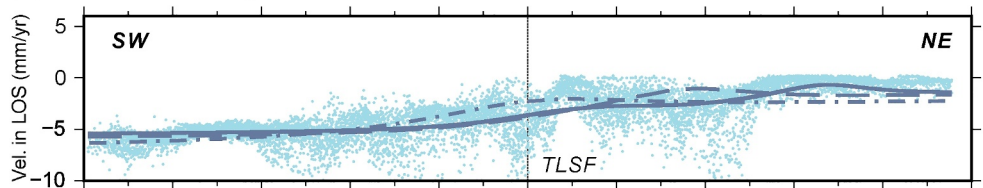
3.2. Setting the Priors

In the Bayesian framework, priors incorporate estimates of the likelihood of a particular variable taking a value based on prior knowledge. We used a uniform distribution within defined bounds for all of the priors, with the upper and lower bounds based on constraints imposed by the geological slip rates, geodetic data and the geometry of the fault system. The oblique convergence across the fault system is defined as the local horizontal shortening ($V_{shorten}$) and shearing (V_{ss}) velocity perpendicular and parallel to the TLSF, respectively (Figure 2). For Model A, the strike-slip rate V_{ss} of the TLSF can take values of 2–8 mm/yr. The horizontal shortening rate $V_{shorten}$ of the thrust faults can take values of 0–10 mm/yr. In Model B, the priors are the same as Model A, but include a south-

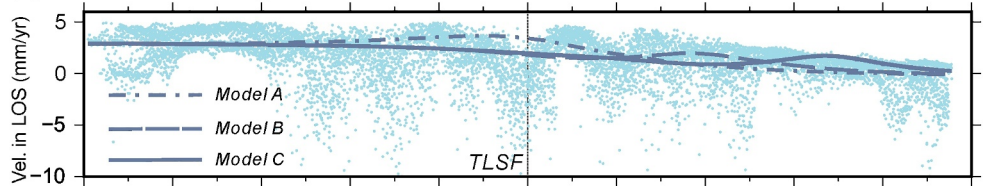
(a) 2-D models



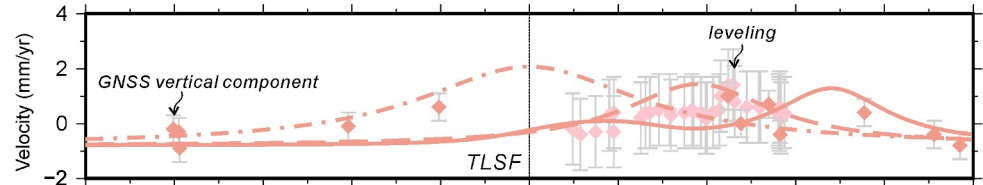
(b) InSAR ascending



(c) InSAR descending



(d) Vertical movement



(e) GNSS horizontal component

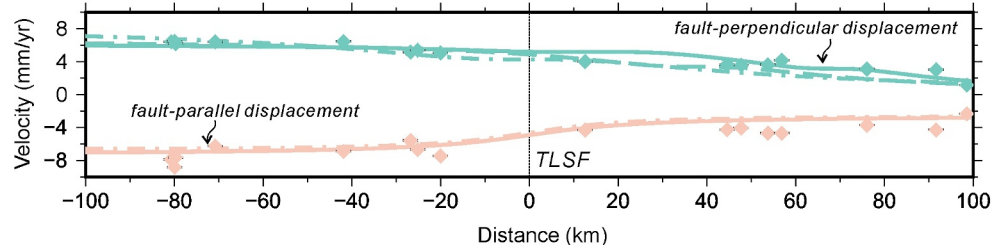


Figure 2. Model setup and data fitting. (a) Sketches of the 2-D models tested (Model A to C) with details of each model variable. Red/black lines denote the creeping/locked fault segments. The dashed red line shows the semi-infinite horizontal dislocation. Panels (b)–(e) show fits between the models and the geodetic data. Lines represent the best-fit model results, blue dots are InSAR observations, and diamonds with error bars are GNSS and leveling data. TLSF is marked by vertical dashed line.

dipping décollement north of the TLSF. The horizontal distance that the creeping décollement extends north of the strike-slip fault HD_{deco} can take values of 2–38 km, and its height is H_{deco} can take values of 0–25 km. For Model C, we added two branches as the proxy of NTLF (with priors HD_{c1} : 0–40 km; H_{c1} : 0–25 km) and NQTF (with priors HD_{c2} : 30–70 km; H_{c2} : 0–25 km), which allow these faults to extend from the décollement to the surface.

4. Results

4.1. Posterior Models

The initial model was manually selected. To mitigate the influence of this initial model choice we discarded the first 30,000 samples of the total 50,000. The mean and standard deviation of the posterior probability distributions (PDFs) for each variable are shown in Table S2 in Supporting Information S1, and the shape of the PDFs are illustrated in Figures S2–S4 in Supporting Information S1 for Models A–C. All parameters exhibit normal distributions in their posterior PDFs and PDFs are narrower than the priors, indicating that the data impose constraints on the range of models that can fit the data (Table S2 in Supporting Information S1).

The fits between the models and the data are good with Model A having a Normalized Root-Mean-Square Error (NRMSE) of 0.50, Model B has a NRMSE of 0.47 and Model C an NRMSE of 0.44. All three models fit the InSAR data and the horizontal GNSS measurements well, with some systematic misfits 40 km north of the range front in the fault-parallel velocities. The most notable difference between the model prediction and the data are in the vertical velocities north of the range front, where each best-fit model predicts a different location for the peak uplift rate. The peak uplift rate is positioned above the tip of the creeping-to-locked transition. Unfortunately, the large uncertainties in the leveling data, and large scatter in the InSAR LOS velocities, are only of limited value for differentiating between models (Text S2 in Supporting Information S1). In the future, more accurate measurements of the vertical velocities across the Qilian Shan range front will be important for placing tighter constraints on the creeping-to-locked transition on faults in the region.

The steady-state creep rate of TLSF V_{ss} is in the range 4.2–4.7 mm/yr for Models A–C, which is similar to the Late Quaternary slip rates (Guo et al., 2020; Jiang et al., 2017; Zheng et al., 2013). The locking depth on the TLSF across all models is 15 ± 1.5 km (Table S2 in Supporting Information S1). This result is consistent with previous studies that only modeled the fault-parallel velocity field around the Qilian-Haiyuan fault and did not consider the thrusts (P. He et al., 2023; Huang et al., 2022; Y. Li et al., 2017; Liu et al., 2022; Qiao et al., 2021). The total shortening rate across the fault system is 9 mm/yr in Model A and 6.3 mm/yr in Model B and Model C.

4.2. Evaluating Model Complexity and Data Fitting

With the increasing number of variables needed to define Model A–C there was only a slight decrease from 0.5 to 0.44 in the NRMSE (Figure 3). To establish whether the change in NRMSE is significant, we used the Akaike Information Criterion (AIC):

$$AIC = 2k + n \ln \left(\frac{RMS}{\sqrt{n}} \right),$$

where k is the number of free parameters of the model and n is the number of geodetic data points (Akaike, 1974). A smaller AIC for a model with more variables suggests that the improvement in data fitting validates the usage of a more complex model. We find that the AIC of Model A is smaller than that of Model B and Model C, suggesting Model A is the optimal model of the three to explain the geodetic observations (Figure 3). Therefore, including the possibility of creep on a décollement and on splay faults within the fold-thrust belt is not justified given the data and its uncertainties. A set of synthetic tests in which we forward model the surface deformation due to creep on the décollement north of the TLSF and the splay thrusts supports the conclusion that these faults are unlikely to be creeping at the late Quaternary slip rate (see more detail in Text in Supporting Information S1; Figures S11–S16 in Supporting Information S1).

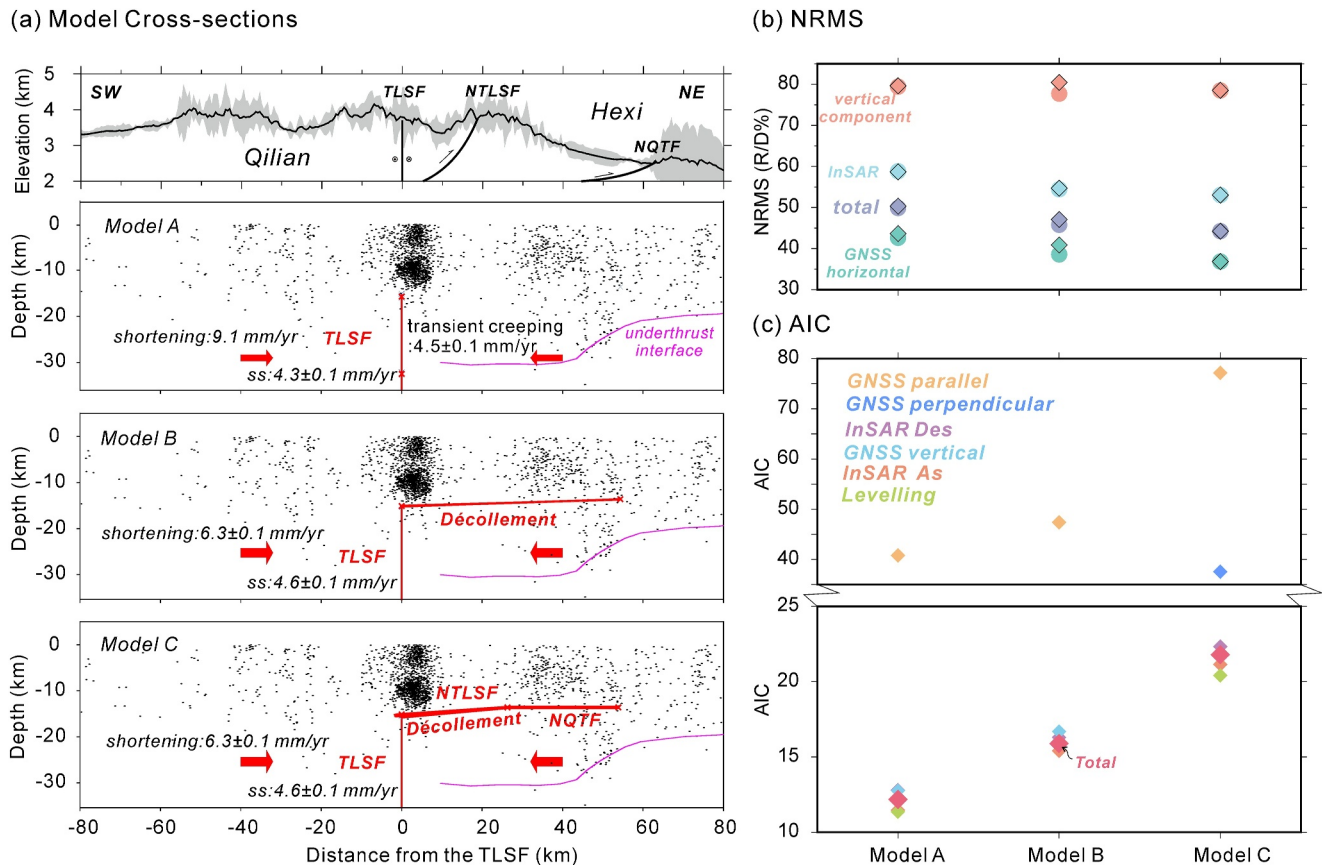


Figure 3. Cross-sections of topography and the creeping faults in models A-C. (a) Topography, model structures, relocated earthquakes (Xia et al., 2021), and the modeled creeping fault geometries in the northern Qilian region (b), (c) Compares NRMS and Akaike Information Criterion values for the different models A-C. The different symbols show results with different data weightings (InSAR:horizontal_GNSS:vertical = 1:20:20 [color-filled diamonds] or 1:20:0 [color-filled circles]).

4.3. Limitations of the Modeling

We chose to model the velocity field across the range front as being due to the elastic strain accumulating around a localized zone of shear because strain at the surface is also localized onto a small number of narrow fault zones. If the interseismic deformation were in fact caused by a series of sub-parallel shear zones or distributed ductile flow at depth, then the geometry and slip rate on the shear zone derived from our modeling will be incorrect in detail.

5. Discussion

5.1. Kinematics, Seismicity, and Long-Term Deformation

Our preferred kinematic model (Model A) indicates that elastic strain is accumulating above a depth of 15 km within the fold-thrust belt of the northern Qilian Shan. The point at which strain is accumulating fastest is the creeping-to-locked transition directly beneath the TLSF. Microseismicity in the region clusters around the inferred creeping-to-locked transition, whilst elsewhere seismicity is broadly distributed throughout the fold-thrust belt north of the TLSF (Figure 3; Xia et al., 2021). Notably, there is no evidence for seismicity clustering at the down-dip edge of the creeping-to-locked transition on the décollement in Model B, or along the shallow thrust faults within the fold-thrust belt (i.e., NTLSF and NQTF) from Model C. We interpret the lack of clustered seismicity north of the TLSF to support the inference that there is only a single creeping-to-locked transition in this region.

Although the kinematic model and seismicity does not require any creep on shallow thrust faults during the interseismic period, there is geological and geomorphological evidence that the thrust faults separating the Qilian Shan and Alashan are active and have accommodated tens of kilometers of crustal shortening in the Cenozoic

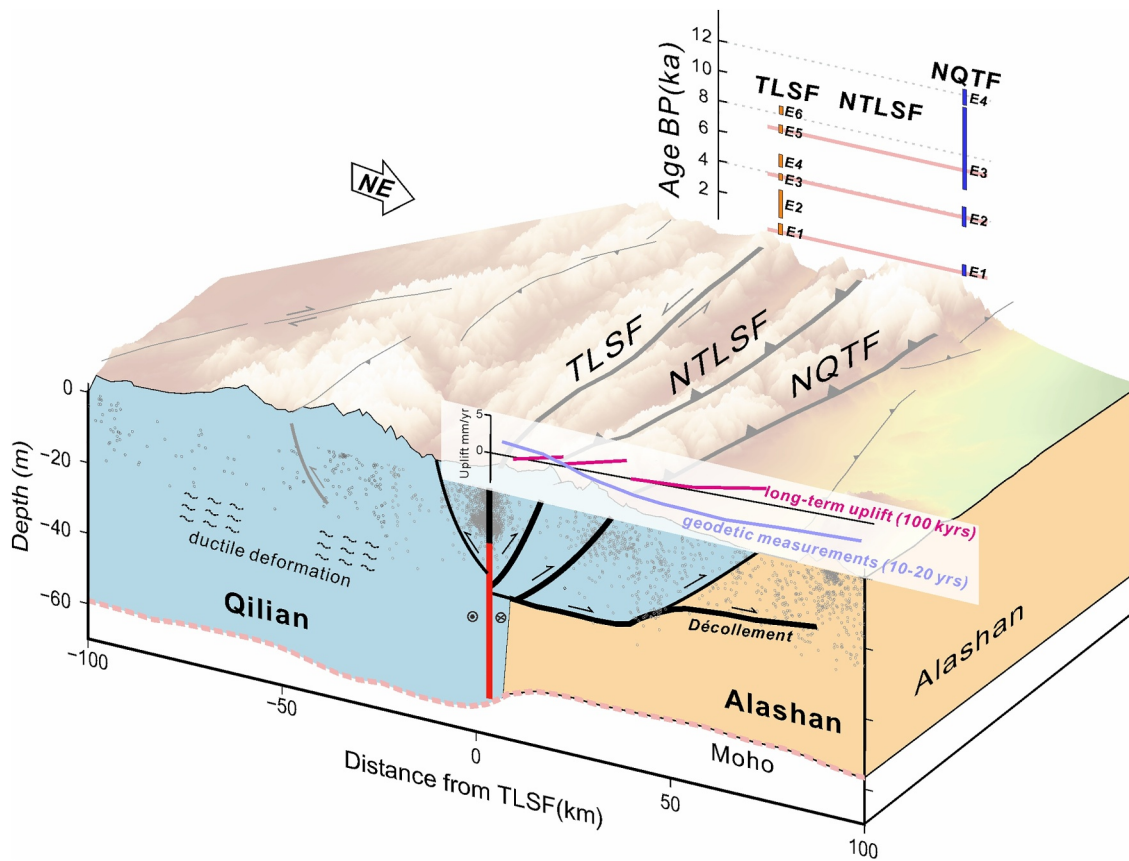


Figure 4. A 3-D block model of the Northern Qilian fault system. Seismicity is shown as gray circles (Xia et al., 2021), and the Moho is taken from (Shen et al., 2017). Locked faults are shown as black lines and creeping faults as red lines. The bold faults are those included in our models. Includes insights into long-term deformation (e. g., Lamb, 2018) and paleo-earthquake records (Z. Li et al., 2022).

(Gaudemer et al., 1995; Meyer et al., 1998; Zuza et al., 2016). In essence, the short-term geodetic measurements do not reflect the kinematics of the locked parts of the thrusts in the northern Qilian Shan over geological timescales (see also Herman et al., 2023; Lamb, 2021; Lamb & Smith, 2013).

5.2. Comparison to Previous Kinematic Models

Allen et al. (2017) previously investigated the kinematics of strain partitioning in the northern Qilian Shan ~150 km to north-west of our data profile. They found that the interseismic horizontal velocity field could be fit by oblique creep on a shallow décollement dipping toward the south that is locked above 26 ± 8 km depth. Our kinematic model is similar to that of Allen et al. (2017) in that all the shallow thrust faults are locked. However, our models infer a shallower depth for the creeping-to-locked transition of 15 km. Our modeling is not consistent with a dipping décollement because the velocity field contains only a small change in the vertical velocity across the range front. Our shallower locking depth could be related to the lateral variations in the structure of the northern Qilian Shan. In the west, the oblique convergence is accommodated by a series of thrust faults merging into a deep décollement (e.g., Meyer et al., 1998), whilst in the east the convergence is accommodated by a “flower structure” (e.g., Gaudemer et al., 1995; G. W. Wu et al., 2023; Figure 4).

5.3. Implications for Multi-Fault Earthquakes and Seismic Hazard

The northern Qilian strain-partitioned faults system (i.e., the TLSF, NTLFSF and NQTF) has previously ruptured in large multi-fault earthquakes (Figure 4; Gao et al., 2022; Z. Li et al., 2022). A key result of our modeling is that this fault system is being simultaneously loaded by a single creeping fault. The shallow (<15 km), locked fault segments that lie above the creeping segment may all fail together as, by virtue of being loaded by the same source of creep, the state of stress at the base of each fault is similar where they sole into one structure. Future ruptures

could potentially occur at any location in the fold-thrust belt (Guo et al., 2020; Mary et al., 2013; Yagupsky et al., 2014), but multi-fault ruptures would be expected to initiate at the creeping-to-locked transition and rupture up-dip. There are no resolvable creeping patches on the décollement that could act as a barrier to rupture propagation between faults once a rupture initiates. Our observations are consistent with the view that multi-fault earthquakes are more common in tectonic settings where the long-term deformation includes a diverse array of kinematically different faults, but the short-term deformation can be explained by a single, deep source of creep.

6. Conclusion

We have shown that geodetic estimates of the interseismic velocity field in the northern Qilian Shan can provide constraints on the kinematics of strain partitioning. Given the data available, we find that thrust faults along the margins of the range front are locked and are being loaded by a creeping décollement. There is no robust geodetic evidence for creep beneath the fold-thrust belt itself. The strike-slip fault within the range interior is likely being loaded by creep on a vertical shear zone that cuts through the Qilian crust. Seismicity in the fold-thrust belt is distributed, whilst seismicity beneath the Qilian-Haiyuan strike-slip fault is concentrated at the geodetically-inferred creeping-to-locked transition. We suggest that, because the whole fold-thrust belt is simultaneously accumulating elastic strain, faults in the northern Qilian Shan may be able to rupture in large magnitude multi-fault earthquakes.

Conflict of Interest

The authors declare no conflicts of interest relevant to this study.

Data Availability Statement

The data (InSAR, GNSS, leveling data) and synthetic modeling script used in this paper have been shared on Zenodo (Y. Zhang, Chen et al., 2023; Y. Zhang, Wimpenny et al., 2023). The Flower2D code is available from the Github (Daout, 2023). Maps were created by using Generic Mapping Tools version 6 (Wessel et al., 2019).

Acknowledgments

The authors wish to thank Dr. Yanchuan Li and Dr. Haibo Yang for useful discussions. We also thank the Editor, Dr. Hanna Elston and one anonymous reviewer for their helpful comments. Prof. Wenyu Gong is thanked for her constructive comments. Yingfeng Zhang was funded by the National Natural Science Foundation of China (Grant 42204007) and the National Key Laboratory for Earthquake Dynamics (Grant LE-21-A06). Luca Dal Zilio was supported by the EU project “A Digital Twin for Geophysical Extremes” (DT-GEO) (101058129) and the European Research Council Synergy Grant “Fault Activation and Earthquake Rupture” (FEAR) (856559). SW was supported by COMET, which is the NERC Centre for the Observation and Modeling of Earthquakes, Volcanoes and Tectonics, a partnership between UK Universities and the British Geological Survey.

References

- Akaike, H. (1974). A new look at the statistical model identification. *IEEE Transactions on Automatic Control*, 19(6), 716–723. <https://doi.org/10.1109/tac.1974.1100705>
- Allen, M. B., Walters, R. J., Song, S., Saville, C., De Paola, N., Ford, J., et al. (2017). Partitioning of oblique convergence coupled to the fault locking behavior of fold-and-thrust belts: Evidence from the Qilian Shan, northeastern Tibetan Plateau. *Tectonics*, 36(9), 1679–1698. <https://doi.org/10.1002/2017TC004476>
- Avouac, J. P. (2015). From geodetic imaging of seismic and aseismic fault slip to dynamic modeling of the seismic cycle. *Annual Review of Earth and Planetary Sciences*, 43(1), 233–271. <https://doi.org/10.1146/annurev-earth-060614-105302>
- Dal Zilio, L., Hetényi, G., Hubbard, J., & Bollinger, L. (2021). Building the Himalaya from tectonic to earthquake scales. *Nature Reviews Earth & Environment*, 2(4), 251–268. <https://doi.org/10.1038/s43017-021-00143-1>
- Dal Zilio, L., Jolivet, R., & van Dinther, Y. (2020). Segmentation of the main Himalayan thrust illuminated by Bayesian inference of interseismic coupling. *Geophysical Research Letters*, 47(4), e2019GL086424. <https://doi.org/10.1029/2019GL086424>
- Daout, S. (2023). simondaout/Flower2d [Software]. *GitHub*. <https://github.com/simondaout/Flower2d>
- Daout, S., Barbot, S., Peltzer, G., Doin, M. P., Liu, Z., & Jolivet, R. (2016). Constraining the kinematics of metropolitan Los Angeles faults with a slip-partitioning model. *Geophysical Research Letters*, 43(21), 11–192. <https://doi.org/10.1002/2016GL071061>
- Daout, S., Jolivet, R., Lasserre, C., Doin, M.-P., Barbot, S., Tapponnier, P., et al. (2017). Along-strike variations of the partitioning of convergence across the Haiyuan fault system detected by InSAR. *Geophysical Journal International*, 205(1), 536–547. <https://doi.org/10.1093/gji/ggw028>
- Gao, F., Zielke, O., Han, Z., Guo, P., Gai, H., & Dai, C. (2022). Faulted landforms, slip-rate, and tectonic implications of the eastern Lenglongling fault, northeastern Tibetan Plateau. *Tectonophysics*, 823, 229195. <https://doi.org/10.1016/j.tecto.2021.229195>
- Gaudemer, Y., Tapponnier, P., Meyer, B., Peltzer, G., Guo, S., Chen, Z., et al. (1995). Partitioning of crustal slip between linked, active faults in the eastern Qilian Shan, and evidence for a major seismic gap, the ‘Tianzhu gap’, on the western Haiyuan Fault, Gansu (China). *Geophysical Journal International*, 120(3), 599–645. <https://doi.org/10.1111/j.1365-246x.1995.tb01842.x>
- Guo, P., Han, Z., Gao, F., Zhu, C., & Gai, H. (2020). A new tectonic model for the 1927 M8.0 Gulang earthquake on the NE Tibetan Plateau. *Tectonics*, 39(9), e2020TC006064. <https://doi.org/10.1029/2020TC006064>
- He, P., Liu, C., Wen, Y., Hu, X., Ding, K., & Xu, C. (2023). The 2022 Mw 6.6 Menyuan earthquake in the Northwest margin of Tibet: Geodetic and seismic evidence of the fault structure and slip behavior of the Qilian–Haiyuan strike-slip fault. *Seismological Research Letters*, 94(1), 26–38. <https://doi.org/10.1785/0220220192>
- He, W. G., Yuan, D. Y., Ge, W. P., & Luo, H. (2010). Determination of the slip rate of the Lenglongling fault in the middle and eastern segments of the Qilian Mountain active fault zone (in Chinese with English abstract). *Earthquake*, 30(1), 131–137.
- Herman, M. W., Furlong, K. P., & Benz, H. M. (2023). Substantial upper plate faulting above a shallow subduction megathrust earthquake: Mechanics and implications of the surface faulting during the 2016 Kaikoura, New Zealand, earthquake. *Tectonics*, 42(5), e2022TC007645. <https://doi.org/10.1029/2022TC007645>

- Huang, Z., Zhou, Y., Qiao, X., Zhang, P., & Cheng, X. (2022). Kinematics of the ~ 1000 km Haiyuan fault system in northeastern Tibet from high-resolution Sentinel-1 InSAR velocities: Fault architecture, slip rates, and partitioning. *Earth and Planetary Science Letters*, 583, 117450. <https://doi.org/10.1016/j.epsl.2022.117450>
- Jiang, W. L., Han, Z. J., Guo, P., Zhang, J. F., Jiao, Q. S., Kang, S., & Tian, Y. (2017). Slip rate and recurrence intervals of the east Lenglongling Fault constrained by morphotectonics: Tectonic implications for the NE Tibetan Plateau. *Lithosphere*, 9(3), 417–430. <https://doi.org/10.1130/L597.1>
- Lamb, S. (2021). The relation between short- and long-term deformation in actively deforming plate boundary zones. *Philosophical Transactions of the Royal Society A*, 379(2193), 20190414. <https://doi.org/10.1098/rsta.2019.0414>
- Lamb, S., Arnold, R., & Moore, J. D. P. (2018). Locking on a megathrust as a cause of distributed faulting and fault-jumping earthquakes. *Nature Geoscience*, 11, 871–875. <https://doi.org/10.1038/s41561-018-0230-5>
- Lamb, S., & Smith, E. (2013). The nature of the plate interface and driving force of interseismic deformation in the New Zealand plate-boundary zone, revealed by the continuous GPS velocity field. *Journal of Geophysical Research: Solid Earth*, 118(6), 3160–3189. <https://doi.org/10.1002/jgrb.50221>
- Lasserre, C., Gaudemer, Y., Tapponnier, P., Mériaux, A. S., Van der Woerd, J., Daoyang, Y., et al. (2002). Fast late pleistocene slip rate on the Leng Long Ling segment of the Haiyuan fault, Qinghai, China. *Journal of Geophysical Research*, 107(B11), ETG 4-1–ETG 4-15. <https://doi.org/10.1029/2000JB000060>
- Li, Y., Shan, X., Qu, C., Zhang, Y., Song, X., Jiang, Y., et al. (2017). Elastic block and strain modeling of GPS data around the Haiyuan-Liupanshan fault, northeastern Tibetan Plateau. *Journal of Asian Earth Sciences*, 150, 87–97. <https://doi.org/10.1016/j.jseae.2017.10.010>
- Li, Z., Xu, X., Tapponnier, P., Chen, G., Ren, J., Li, K., et al. (2022). Long, regular return of four large earthquakes on Qilian Shan's Minle-Damayong frontal thrust (NE Tibet): Partial clustering with great events on the Leng Long Ling fault? *Journal of Geophysical Research: Solid Earth*, 127(5), e2021JB022800. <https://doi.org/10.1029/2021JB022800>
- Liu, L., Zhuang, W., Ji, L., Zhu, L., & Jiang, F. (2022). Fault locking of the Qilian–Haiyuan fault zone before the 2022 Menyuan Ms6.9 earthquake and its seismic hazards in the future. *Frontiers of Earth Science*, 10, 929597. <https://doi.org/10.3389/feart.2022.929597>
- Luo, H., & Wang, T. (2022). Strain partitioning on the western Haiyuan fault system revealed by the adjacent 2016 Mw5.9 and 2022 Mw6.7 Menyuan earthquakes. *Geophysical Research Letters*, 49(16), e2022GL099348. <https://doi.org/10.1029/2022GL099348>
- Mary, B., Maillot, B., & Leroy, Y. M. (2013). Deterministic chaos in frictional wedges revealed by convergence analysis. *International Journal for Numerical and Analytical Methods in Geomechanics*, 37(17), 3036–3051. <https://doi.org/10.1002/nag.2177>
- McCaffrey, R. (1988). Active tectonics of the eastern Sunda and Banda arcs. *Journal of Geophysical Research*, 93(B12), 15163–15182. <https://doi.org/10.1029/jb093ib12p15163>
- Meyer, B., Tapponnier, P., Bourjot, L., Metivier, F., Gaudemer, Y., Peltzer, G., et al. (1998). Crustal thickening in Gansu-Qinghai, lithospheric mantle subduction, and oblique, strike-slip controlled growth of the Tibet plateau. *Geophysical Journal International*, 135(1), 1–47. <https://doi.org/10.1046/j.1365-246x.1998.00567.x>
- Murphy, M. A., Taylor, M. H., Gosse, J., Silver, C. R. P., Whipp, D. M., & Beaumont, C. (2014). Limit of strain partitioning in the Himalaya marked by large earthquakes in western Nepal. *Nature Geoscience*, 7(1), 38–42. <https://doi.org/10.1038/ngeo2017>
- Ou, Q., Daout, S., Weiss, J. R., Shen, L., Lazecký, M., Wright, T. J., & Parsons, B. E. (2022). Large-scale interseismic strain mapping of the NE Tibetan Plateau from Sentinel-1 interferometry. *Journal of Geophysical Research: Solid Earth*, 127(6), e2022JB024176. <https://doi.org/10.1029/2022JB024176>
- Qiao, X., Qu, C., Shan, X., Zhao, D., & Liu, L. (2021). Interseismic slip and coupling along the Haiyuan fault zone constrained by InSAR and GPS measurements. *Remote Sensing*, 13(16), 3333. <https://doi.org/10.3390/rs13163333>
- Sanderson, D. J., & Marchini, W. R. D. (1984). Transpression. *Journal of Structural Geology*, 6(5), 449–458. [https://doi.org/10.1016/0191-8141\(84\)90058-0](https://doi.org/10.1016/0191-8141(84)90058-0)
- Schütt, J. M., & Whipp, D. M. (2020). Controls on continental strain partitioning above an oblique subduction zone, Northern Andes. *Tectonics*, 39(4), e2019TC005886. <https://doi.org/10.1029/2019TC005886>
- Segall, P. (2010). *Earthquake and volcano deformation*. Princeton University Press.
- Shen, X., Kim, Y., & Gan, W. (2017). Lithospheric velocity structure of the northeast margin of the Tibetan Plateau: Relevance to continental geodynamics and seismicity. *Tectonophysics*, 712, 482–493. <https://doi.org/10.1016/j.tecto.2017.06.022>
- Shi, X., Wang, Y., Liu-Zeng, J., Weldon, R., Wei, S., Wang, T., & Sieh, K. (2017). How complex is the 2016 Mw 7.8 Kaikoura earthquake, south Island, New Zealand. *Science Bulletin*, 62(5), 309–311. <https://doi.org/10.1016/j.scib.2017.01.033>
- Wang, M., & Shen, Z. K. (2020). Present-day crustal deformation of continental China derived from GPS and its tectonic implications. *Journal of Geophysical Research: Solid Earth*, 125(2), e2019JB018774. <https://doi.org/10.1029/2019JB018774>
- Wessel, P., Luis, J. F., Uieda, L., Scharroo, R., Wobbe, F., Smith, W. H. F., & Tian, D. (2019). The generic mapping tools version 6. *Geochemistry, Geophysics, Geosystems*, 20(11), 5556–5564. <https://doi.org/10.1029/2019gc008515>
- Wu, G. W., Xiong, X. S., Gao, R., Chen, X. H., Li, Y. K., Wang, G., & Ren, H. D. (2023). Moho depth of the Qilian orogen revealed by wideangle reflection/refraction profiles. *Reviews of Geophysics and Planetary Physics*, 54(2), 109–119. (in Chinese). <https://doi.org/10.19975/j.dqyx.2021-067>
- Wu, Y., Zheng, Z., Nie, J., Chang, L., Su, G., Yin, H., et al. (2022). High-precision vertical movement and three-dimensional deformation pattern of the Tibetan plateau. *Journal of Geophysical Research: Solid Earth*, 127(4), e2021JB023202. <https://doi.org/10.1029/2021JB023202>
- Xia, S. R., Shi, L., Li, Y. H., & Guo, L. H. (2021). Velocity structures of the crust and upper most mantle beneath the northeastern margin of Tibetan Plateau revealed by double difference tomography. *Chinese Journal of Geophysics*, 64(9), 3194–3206. <https://doi.org/10.6038/cjg202100514>
- Xiong, J., Li, Y., Zhong, Y., Lu, H., Lei, J., Xin, W., et al. (2017). Latest Pleistocene to Holocene thrusting recorded by a flight of strath terraces in the eastern Qilian Shan, NE Tibetan plateau. *Tectonics*, 36(12), 2973–2986. <https://doi.org/10.1002/2017TC004648>
- Yagupsky, D. L., Brooks, B. A., Whipple, K. X., Duncan, C. C., & Bevis, M. (2014). Distribution of active faulting along orogenic wedges: Minimum-work models and natural analogue. *Journal of Structural Geology*, 66, 237–247. <https://doi.org/10.1016/j.jsg.2014.05.025>
- Ye, Z., Gao, R., Li, Q., Zhang, H., Shen, X., Liu, X., & Gong, C. (2015). Seismic evidence for the North China plate underthrusting beneath northeastern Tibet and its implications for plateau growth. *Earth and Planetary Science Letters*, 426, 109–117. <https://doi.org/10.1016/j.epsl.2015.06.024>
- Yuan, D. Y., Ge, W. P., Chen, Z. W., Li, C. Y., Wang, Z. C., Zhang, H. P., et al. (2013). The growth of northeastern Tibet and its relevance to large scale continental geodynamics: A review of recent studies. *Tectonics*, 32(5), 1358–1370. <https://doi.org/10.1002/tect.200>
- Zhang, P., Shen, Z., Wang, M., Gan, W., Bürgmann, R., Molnar, P., et al. (2004). Continuous deformation of the Tibetan Plateau from global positioning system data. *Geology*, 32(9), 809–812. <https://doi.org/10.1130/G20554.1>

- Zhang, Y., Chen, J., Gong, W., Han, N., Liu, Y., & Shan, X. (2023). Geodetic modelling of the 2022 M_w 6.6 Menyuan Earthquake: Insight into the strain-partitioned northern Qilian Shan fault system and implications for regional tectonics and seismic hazards. *Geophysical Journal International*, 233(3), 1987–2003. <https://doi.org/10.1093/gji/ggad012>
- Zhang, Y., Shan, X., Zhang, G., Zhong, M., Zhao, Y., Wen, S., & Zhao, D. (2020). The 2016 M_w 5.9 Menyuan earthquake in the Qilian orogen, China: A potentially delayed depth-segmented rupture following from the 1986 M_w 6.0 Menyuan earthquake. *Seismological Research Letters*, 91(2A), 758–769. <https://doi.org/10.1785/0220190168>
- Zhang, Y., Wimpenny, S., Dal, Z. L., & Shan, X. (2023). Strain partitioning and fault kinematics in the Northern Qilian Shan (NE Tibet) determined from Bayesian inference of geodetic data [dataset]. *Zenodo*. <https://doi.org/10.5281/zenodo.8433179>
- Zhao, Q., Chen, Q., van Dam, T., She, Y., & Wu, W. (2023). The vertical velocity field of the Tibetan Plateau and its surrounding areas derived from GPS and surface mass loading models. *Earth and Planetary Science Letters*, 609, 118107. <https://doi.org/10.1016/j.epsl.2023.118107>
- Zheng, W., Zhang, P., He, W., Yuan, D., Shao, Y., Zheng, D., et al. (2013). Transformation of displacement between strike-slip and crustal shortening in the northern margin of the Tibetan Plateau: Evidence from decadal GPS measurements and late Quaternary slip rates on faults. *Tectonophysics*, 584, 267–280. <https://doi.org/10.1016/j.tecto.2012.01.006>
- Zhong, Y., Xiong, J., Li, Y., Zheng, W., Zhang, P., Lu, H., et al. (2020). Constraining Late Quaternary crustal shortening in the eastern Qilian Shan from deformed river terraces. *Journal of Geophysical Research: Solid Earth*, 125(9), e2020JB020631. <https://doi.org/10.1029/2020JB020631>
- Zuza, A. V., Cheng, X., & Yin, A. (2016). Testing models of Tibetan Plateau formation with Cenozoic shortening estimates across the Qilian Shan–Nan Shan thrust belt. *Geosphere*, 12(2), 501–532. <https://doi.org/10.1130/GES01254.1>